JOURNAL OF SPACECRAFT AND ROCKETS
Vol. 45, No. 2, March–April 2008

Kinetic and Continuum Simulations of Electromagnetic Control of a Simulated Reentry Flow

Hiroshi Katsurayama,* Masaaki Kawamura,† Atsushi Matsuda,‡ and Takashi Abe§
Japan Aerospace Exploration Agency, Kanagawa 229-8510, Japan

DOI: 10.2514/1.31702

Electromagnetic control of a weakly ionized supersonic rarefied argon flow past a magnetized blunt body is simulated using the direct simulation Monte Carlo method with Ohm's law. According to the corresponding experiment using an arcjet wind tunnel, the Knudsen and Mach numbers of the flow are, respectively, 0.05 and 1.7, and a dipolar magnetic field for which the maximum value is about 0.4 T is imposed around the body. Although the Hall and ion slip effects are estimated to be significant in the flow, the present computations ignore these effects, for simplicity. The result is compared not only with the experimental result but also with the simulated result using Navier–Stokes computation. The kinetic (direct simulation Monte Carlo) and continuum (Navier–Stokes) simulations produced almost identical translational temperature distributions with application and with no application of a magnetic field. Results show that the continuum approximation is acceptable to predict the flow structure. Both simulations roughly reproduced the measured shock layer enlargement resulting from the Lorentz force against the flow direction and predicted the resulting reduction of the net heat load on the body. In addition, the direct simulation Monte Carlo correctly predicted the drag measured in the case of the not-applied field and verified the electromagnetic drag increase measured qualitatively in the case of the applied field; the electromagnetic effect increases the total drag, because the reaction of the generated Lorentz force prominently exceeds the slight decrease of aerodynamic drag caused by the shock layer enlargement.

I. Introduction

REENTRY vehicles are exposed to severe convective heating, attributable to a high-enthalpy flow past them. A passive system with a heat-resistant or adiabatic material has been employed to protect the vehicles from aerodynamic heating. However, the lack of reusability and low reliability of such a thermal protection system persist as obstacles to cost and risk reductions of space transportation systems. An alternative to existing thermal protection systems can be achieved by actively controlling a partially ionized flow past the vehicle through an applied magnetic field [1–3]. Figure 1 shows a schematic view of such electromagnetic flow control. A magnet embedded in a blunt body forms a dipolarlike magnetic field $\boldsymbol{B}$ around the body, and a circumferential current J_θ is induced according to Ohm's law through the interaction between $\boldsymbol{B}$ and the weakly ionized flow v behind a bow shock. The electromagnetic effect generates the Lorentz force $\boldsymbol{J} \times \boldsymbol{B}$ against the flow direction, and the shock standoff distance is enlarged; the effect reduces aerodynamic heating and increases aerodynamic drag, because the effective radius of curvature of the body increases from the viewpoint of the bow shock (in practice, $\boldsymbol{J} \times \boldsymbol{B}$ acting on the fluid exerts a reaction force on the magnet [3]). The slowdown of flight velocity attributable to this increased drag drastically reduces the heating accumulated throughout an entire flight path [4,5].

To make the electromagnetic flow control effective, the magnetic interaction parameter [6] Q requires a condition by which

$$Q = (\sigma B^2 L)/(\rho_\infty v_\infty) \gtrsim 1 \tag{1}$$

where σ, $\rho_\infty v_\infty$, and L, respectively, represent electric conductivity, the momentum of the flow, and the characteristic length of the body. Many researchers studied this topic in the 1950–1970s theoretically [1–3] and experimentally [7–10], and these early experiments have shown the luminous shock layer enlargement [7,8], heat flux reduction [9], and drag increase [10] through the electromagnetic effect. However, electromagnetic flow control has not been realized, because the applied field required for $Q > 1$ is too strong for actual applications. Nevertheless, recent technological advancements of superconductive materials have made it possible to develop a magnet with the necessary strength: an on-board magnet can be applied to an active thermal protection system for a reentry vehicle. For those reasons, the concept of the electromagnetic flow control has been revisited, and experimental [11–13] and numerical [14–16] studies have been carried out in recent years.

Although these numerical studies using the continuum approach [Navier–Stokes (NS) equations] have qualitatively verified the luminous shock layer enlargement [7,8] and heat flux reduction [9] reported in the early experiments, quantitative measurements have been required to validate the electromagnetic effect. Takizawa et al. [11] and Matsuda et al. [12] recently quantitatively measured translational temperature distributions around a blunt body with an embedded permanent magnet using an absorption spectroscopy technique. In the experiment, the body is located in a weakly ionized argon supersonic flow of $Q \approx 14$ generated by an arcjet wind tunnel. The measured shock layer enlargement was verified qualitatively using a NS computation [17], but the continuum approximation is probably unacceptable, because the Knudsen number K_n of the flow is estimated to be 0.05, based on the body diameter.

In addition to the early experimental study [10], Kawamura et al. [13] recently measured the drag force exerted on the body using a pendulum apparatus in the same flow condition shown in [12] and obtained an apparent drag increase attributable to applying a magnetic field. Although the drag increase is expected to be caused by the reaction of the Lorentz force exerted on a magnet [3], numerical verification is necessary to confirm it.

Presented as Paper 1439 at the 45th AIAA Aerospace Sciences Meeting and Exhibit, Reno, NV, 8–11 January 2007; received 19 April 2007; accepted for publication 6 September 2007.

*Postdoctoral Researcher, Institute of Space and Astronautical Science, Space Transportation Engineering Division, 3-1-1 Yoshinodai, Sagamihara; katsurayama@isas.jaxa.jp. Member AIAA.

†Currently Graduate Student, Department of Aeronautics and Astronautics, University of Tokyo, 7-3-1 Hongo, Bunkyo-ku.

‡Postdoctoral Researcher, Institute of Space and Astronautical Science, Space Transportation Engineering Division. Member AIAA.

§Professor, Institute of Space and Astronautical Science, Space Transportation Engineering Division. Associate Fellow AIAA.

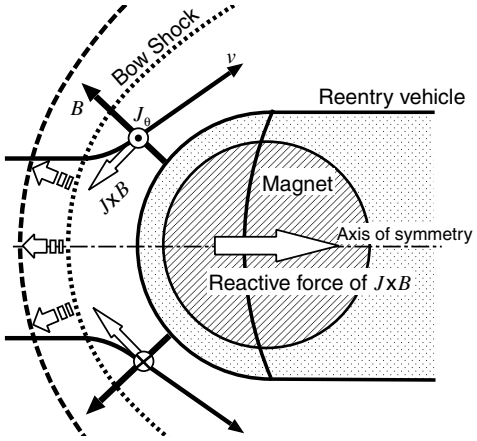

Fig. 1 Schematic view of electromagnetic flow control.

The objectives of this study are to assess rarefied effects in the flow using a kinetic approach [direct simulation Monte-Carlo (DSMC) method] and to verify the electromagnetic drag increase numerically. The DSMC prediction is compared with the result of NS computation performed for the same flow condition. In the simulations, the Lorentz force is modeled using simplified Ohm's law: charged particles are assumed to be a continuum. Subsequently, the resulting shock layer enlargement and drag increase are compared with the experimental results [12,13].

II. Flow Conditions and the Physical Model

Table 1 shows flow conditions measured at a location on the central axis of the arcjet plume [11,12], at which a spherical blunt body of 22 mm in diameter was set up. Although the plume diameter at the setup location is only about twice as large as that of the body, the present study ignores the finite radius and nonuniformity of the plume and assumes the body to be exposed to the uniform axisymmetric flow with the condition of Table 1.

A dipolar magnetic field $\boldsymbol{B} = (B_z, B_r, 0)^t$ is applied to the center of the spherical head, as shown in Fig. 2; it has the maximum value of $B_0 = 0.36$ T at the stagnation point of the body. As the figure depicts, the axial, radial, and circumferential coordinates are expressed, respectively, as z, r, and θ.

The characteristic times of the flow τ_f, chemical reaction τ_r, and temperature relaxation τ_t are defined, respectively, as

$$\tau_f = L/v \tag{2}$$

$$\tau_r = \left(k_f n_n - k_b n_e^2\right)^{-1} \tag{3}$$

$$\tau_t = [2(m_e/m_n)(1 - T/T_e)(\nu_{\text{en}} + \nu_{\text{ei}})]^{-1} \tag{4}$$

Table 1 Conditions of the arcjet plume [11,12][a]

Gas	Ar
Characteristic length L, mm (diameter of the blunt body)	22
Knudsen number K_n	0.05
Mach number M_∞	1.7
Flow velocity v_∞, m/s	1097
Heavy particle temperature T_∞, K	1200
Electron temperature $T_{e,\infty}$, K	$\approx$6100 [11][a]
Neutral particle number density $n_{n,\infty}$, m^{-3}	2.05×10^{21}
Electron number density $n_{e,\infty}$, m^{-3}	$\approx 1 \times 10^{19}$
Ionization degree α_∞	$\approx$0.5%
Static pressure p_∞, Pa	34
Magnetic flux density at the stagnation point B_0, T	0.36
Electric conductivity σ_∞, S/m	731
Magnetic interaction parameter Q	14

[a]Only T_e is taken from [11].

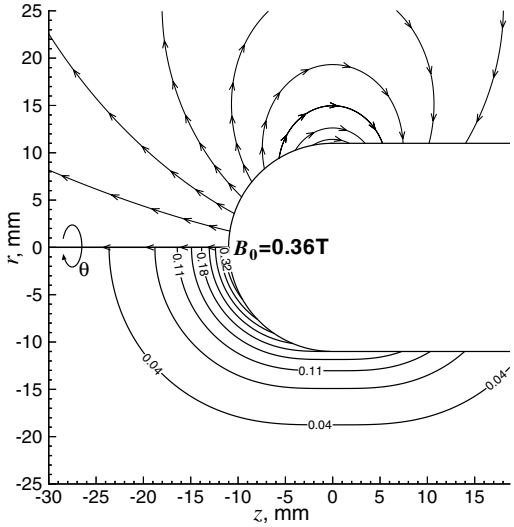

Fig. 2 Applied magnetic field: streamlines (top) and magnitude (bottom).

Herein, k_f and k_b are forward and backward rate constants [18] of the reaction $\text{Ar} + \text{e} \rightleftarrows \text{Ar}^+ + \text{e} + \text{e}$; m_e and m_n are masses of electron and argon; and ν_{en} and ν_{ei}, respectively, represent the electron–atom and electron–ion collisional frequencies [18]. Using the flow conditions listed in Table 1, the ratios of τ_r and τ_t to τ_f are estimated as

$$(\tau_r/\tau_f)_\infty = 2 \times 10^7, \qquad (\tau_t/\tau_f)_\infty = 6 \tag{5}$$

Consequently, the flow is reasonably assumed to be thermochemically frozen, although energy might be transferred slightly from electrons to heavy particles; ionization degree α and electron temperature T_e are constant in the entire flow, and the gas is treated as an ideal argon gas of

$$\alpha = \alpha_\infty = \text{const}, \qquad T_e = T_{e,\infty} = \text{const} \tag{6}$$

Mean free paths of neutral, ion, and electron particles are estimated, respectively, as $\lambda_{n,\infty} = 1$ mm, $\lambda_{i,\infty} = 0.5$ mm, and $\lambda_{e,\infty} = 1.3$ mm using collision cross sections of neutral–neutral [19], electron–ion [18], electron–neutral [18], and ion–neutral [20,21]; mean free paths of all species are on the same order. In addition, the plasma is quasi neutral, because the mean free paths and L are much larger than the Debye length $\lambda_{D,\infty} = 1.7$ μm. To simulate such rarefied collisional quasi-neutral plasma correctly, Gatsonis and Yin [21] proposed a new comprehensive hybrid (particle–fluid) method, in which neutrals and ions are treated as particles using the DSMC/particle-in-cell (PIC) [22] method and electrons are modeled as a massless fluid. However, the overall structure of the arcjet flow is expected to be insensitive to ion trajectories, because α_∞ is only 0.5%. The analysis in the present study therefore ignores rarefied effects that originate in charged particles, but uses the magnetohydrodynamic (MHD) approximation to estimate current density $\boldsymbol{J}$. The MHD approximation requires the following conditions [6,23] under charge neutrality:

$$\tau_f \gg \omega_p^{-1}, \qquad (\nu_{\text{en}} + \nu_{\text{ei}})^{-1} \tag{7}$$

$$L \gg r_{L,i} \tag{8}$$

where ω_p and $r_{L,i}$ are the plasma frequency and ion Larmor radius. The weakly ionized argon plasma under the present condition satisfies these conditions, because $\tau_f = 20$ μs, $\omega_p^{-1} = 6 \times 10^{-6}$ μs, $(\nu_{\text{en}} + \nu_{\text{ei}})^{-1} \approx \nu_{\text{ei}}^{-1} = 2.5 \times 10^{-3}$ μs, and $r_{L,i} = 0.8$ mm.

In collision-dominant microscopic processes in which collisions interrupt the cyclotron motion of charged particles, electrons diffuse in the θ direction through the effective electric field $E_\theta^* = \boldsymbol{v} \times \boldsymbol{B}$, and the MHD approximation can express this electron flux as the macroscopic $\boldsymbol{J}$ using Ohm's law:

$$\boldsymbol{J} = (J_z, J_r, J_\theta)^t = \sigma \boldsymbol{v} \times \boldsymbol{B} = \sigma(0, 0, v_z B_r - v_r B_z)^t \quad (9)$$

Therein, the Hall and ion slip effects (i.e., the effects of the cyclotron motion of charged particles) and the resulting electric field are ignored for simplicity, even though the $\boldsymbol{E} \times \boldsymbol{B}$ drift resulting from these effects might affect current distribution, because the Hall parameter and ion slip factor are estimated, respectively, as 40 and 10 at the stagnation point, where B becomes maximum.

The electrons diffusing at velocity $v_{e,\theta}$ in the θ direction receive the Lorentz force (i.e., $-ev_{e,\theta}\hat{\boldsymbol{\theta}} \times \boldsymbol{B}$, where e and $\hat{\boldsymbol{\theta}}$ are the elementary charge and the unit vector of the θ direction); they transfer the obtained momentum of $\hat{\boldsymbol{\theta}} \times \boldsymbol{B}$ direction to ions, not neutrals, because ν_{ei} is 100 times larger than ν_{en}. Furthermore, the flow structure changes as a result of the momentum transfer from ions to neutrals. The MHD approximation can express this microscopic momentum transfer simply as the following macroscopic Lorentz force acting on neutrals, because charged particles negligibly contribute to the flow structure, due to $\alpha = 0.5\%$:

$$\boldsymbol{J} \times \boldsymbol{B} = (-J_\theta B_r, J_\theta B_z, 0)^t \quad (10)$$

Under the assumption of the thermochemically frozen flow, σ has a constant value of

$$\sigma_\infty = e^2 n_e / [m_e(\nu_{en} + \nu_{ei})]_\infty = 731 \text{ S/m} \quad (11)$$

in the entire flow, the increase of σ resulting from shock heating is small because M_∞ is only 1.7. In addition, the deformation of $\boldsymbol{B}$ caused by coupling with the flow is negligible because the magnetic Reynolds number $R_{m,\infty}$ is estimated as

$$R_{m,\infty} = \mu_0 \sigma_\infty v_\infty L = 2.2 \times 10^{-2} \ll 1 \quad (12)$$

where μ_0 is the permeability of vacuum.

III. Computational Methods

A. DSMC

Under the assumptions of the continuum approximation of charged particles and the insensitivity of the flow structure to ion trajectories, only trajectories of neutral argon atoms are solved using Bird's [19] axisymmetric DSMC method. Collisions among atoms are computed using Bird's no-time-counter (NTC) method and the variable hard sphere (VHS) [19] model. The VHS model estimates a collision cross section using the following viscosity μ:

$$\mu/\mu_s = (T/T_s)^\omega \quad (13)$$

In the case of an argon gas, T_s, μ_s, and ω, respectively, represent 273 K, 2.177×10^{-5} Ns/m^2, and 0.81 [19].

In the DSMC, a sample particle represents many real particles, and a collisional scheme (the NTC method in this study) probabilistically selects collisional pairs from sample particles in a cell. Consequently, a large statistical error arises if sample particles within a cell are too few. Especially in the axisymmetric DSMC, the cell near the axis contains fewer sample particles than the outer cell, because the axisymmetric cell volume is proportional to the radial location of the cell. This study uses the radial weighing factor method [19] to reduce the large statistical error in the cells near the axis. This method equalizes the number of sample particles within each axisymmetric cell volume by increasing the number of real particles that are represented by a sample particle N_w in proportion to its radial location; that is,

$$\text{if } r > r_0, \; N_w = N_0 r / r_0 \quad (14)$$

$$\text{else } N_w = N_0 \quad (15)$$

where r_0 is a reference radius. A sample particle represents N_0 real particles when it is located in $r \le r_0$. According to Bird's [19] criteria, the present study uses $r_0 = 4$ mm, which is eight times the minimum cell size.

In addition, the DSMC has the tendency to lose weak physical disturbances, because the relative locations of particles in a cell are disregarded in selecting collisional pairs [19]. A collisional pair is selected in a small subcell within a cell to improve this tendency. For analyses of the present study, cells are divided into four subdivisions.

B. NS Computation

Axisymmetric Navier–Stokes equations of an ideal argon flow are solved. A cell-centered finite volume scheme is adopted. Inviscid fluxes are estimated using the advection upstream splitting method (AUSM-DV) scheme [24], and its spatial accuracy is extended to third-order using the monotone upstream-centered scheme for conservation laws approach [25] with Van Albada's limiter [26]. Time integration is performed using the lower–upper Gauss–Seidel (LU-SGS) scheme [27]. The viscous and heat fluxes are estimated using a standard central difference with μ of Eq. (13) and the following thermal conductivity κ, which is deduced from the Prandtl number of an ideal monoatomic gas:

$$\kappa = (15/4)(k_B/m_n)\mu \quad (16)$$

C. Computational Modeling of the Lorentz Force

As described in Sec. II, the present DSMC computation uses the MHD approximation instead of solving trajectories of charged particles; in the particle movement part of the DSMC scheme, particles (neutral) are accelerated through the macroscopic Lorentz force $\boldsymbol{F}$, although it microscopically results from the collisional momentum transfer from ions (accelerated through collisions with electrons) to neutrals. $\boldsymbol{F}$ acting on a particle is assumed to be constant in a cell. Using the time-averaged velocity $\bar{\boldsymbol{v}}$ and number density $\overline{n_n}$ in a cell, $\boldsymbol{F}$ and $\boldsymbol{J}$ are calculated as

$$\boldsymbol{J} = \sigma_\infty \bar{\boldsymbol{v}} \times \boldsymbol{B}, \qquad \boldsymbol{F} = \boldsymbol{J} \times \boldsymbol{B} / (m_n \overline{n_n}) \quad (17)$$

The location $\boldsymbol{x}$ and velocity $\boldsymbol{v}$ of a particle are renewed through

$$\boldsymbol{v}^{n+1} = \boldsymbol{v}^n + \boldsymbol{F}^n \Delta t, \qquad \boldsymbol{x}^{n+1} = \boldsymbol{x}^n + \boldsymbol{v}^n \Delta t + \boldsymbol{F}^n \Delta t^2/2 \quad (18)$$

where n is a time step number and Δt is a time interval.

In the NS computation, the $\boldsymbol{J} \times \boldsymbol{B}$ term is added to the right-hand side in the axial and radial momentum-conservation equations. The circumferential momentum-conservation equation is not solved because of $(\boldsymbol{J} \times \boldsymbol{B})_\theta = 0$. In addition, the Joule heating term $\boldsymbol{J} \cdot \boldsymbol{E}$ does not formally appear in the conservation equation of overall energy (i.e., the sum of internal and kinetic energy), because no electric field $\boldsymbol{E}$ is induced under the present assumption (if the internal energy conservation equation is solved instead of that of overall energy, the Joule heating term $\boldsymbol{J} \cdot \boldsymbol{E}^\times = \boldsymbol{J} \cdot (\boldsymbol{v} \times \boldsymbol{B})$ originating from J_θ appears explicitly in the equation) [6].

D. Computational Grid and Boundary Conditions

Figure 3 shows the computational grid and boundary conditions in the DSMC. The blunt body size is identical to that used in the experiment [12]. At boundaries except for the body surface, particles enter according to the Maxwellian distribution at T_∞ and exit along their trajectories. The diffuse reflection condition at a wall temperature T_w is imposed on the body surface. For lack of available experimental data, T_w is assumed to be 1000 K, which is the meltdown limit of the body material (ceramic). Although $T_w = 300$, 500, and 1000 K were tested, the flow structure was insensitive to T_w. The aerodynamic drag decreases with decreasing T_w, but its variation is within 6% in the tested range of T_w.

In the irregular grid of $z < 0$, the localization method of [28] is used to specify the cell containing a particle. The cell size is roughly equal to a local λ_n.

In the NS computation, the same grid is used, and the no-slip isothermal (at T_w), supersonic inflow, and free outflow conditions are imposed, respectively, on the body surface, left, and upper boundaries. On the right boundary, if the flow on it is subsonic, the pressure on the boundary is specified as p_∞ and other primitive

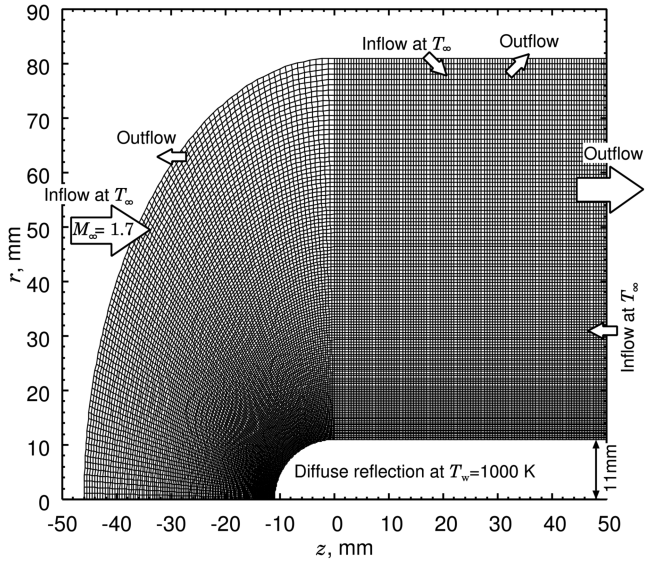

Fig. 3 Computational grid.

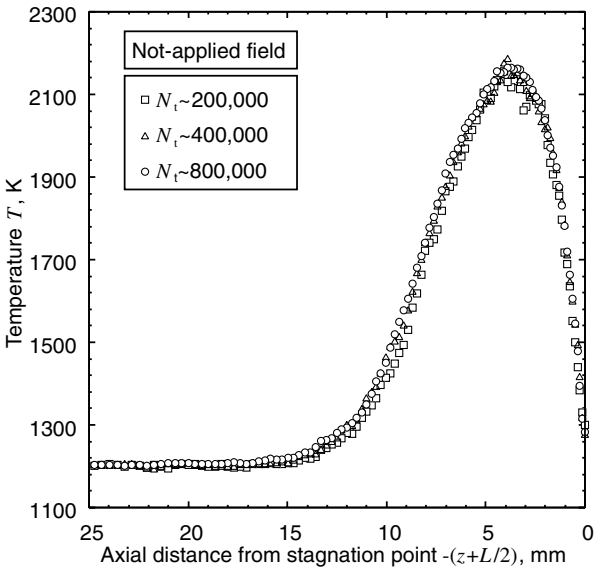

Fig. 4 DSMC solution accuracy: temperature distributions on the axis of symmetry.

values are extrapolated to first order. Otherwise, the supersonic outflow condition is imposed on it.

The gird convergence in the NS computation was investigated through the estimation of the aerodynamic drag coefficient and the net heat load on the body using the original (shown in Fig. 3) and its double-fine grids. The differences between the original and double-fine grids are smaller than 1.5% in cases of both applied and not-applied fields. Moreover, to estimate a heat load correctly, a grid should satisfy the criterion that the cell Reynolds number $R_{e,c}$ is of order one along a body surface. In the original grid, $R_{e,c}$ is from 0.27 (at the stagnation point) to 0.53 (on the cylindrical part of the body) along the body surface. Hence, the resolution of the original grid is adequate for the NS computations.

IV. Results and Discussion

In the DSMC, the total number of sample particles in the computational region becomes steady after approximately 10,000 time steps; then physical properties of particles are accumulated for each of five time steps to obtain the time-averaged solution. The value of Δt is set to 0.2 times the minimum time among the local mean free times or the residence times (ratio of the cell size to the mean particle speed) estimated in each cell. The computation is terminated at 40,000 accumulations. The solution accuracy is verified by varying the total number of sample particles N_t approximately from 200,000 to 800,000 in increments of 200,000 particles. Figure 4 shows the temperature distributions on the axis of symmetry for the case of the not-applied field. $N_t \sim 200,000$ is adequate because the solution remains almost unchanged in the tested range of N_t, but this study used $N_t \sim 800,000$ to obtain clear contours. N_0 in Eq. (15) is 4.25×10^{11} m^{-3} in the case of $N_t \sim 800,000$.

A. Temperature Distribution

Figure 5 shows the temperature contours of the DSMC and NS computations in the case of the not-applied field. Both methods produce almost identical results around the spherical head. This is probably attributable to the low Mach number of the arcjet flow. A visible difference due to a rarefied effect is observed only on the cylindrical part of the body in $z > 0$, because the density on the cylindrical part is approximately 0.2 times of that near the stagnation point.

Figures 6 and 7 show the temperature contours and Lorentz force contours with the directional vector in the case of $B_0 = 0.36$ T. The shock standoff distance increases through the Lorentz force against the flow direction. The difference between both simulations is also negligible. Consequently, the continuum approximation appears to

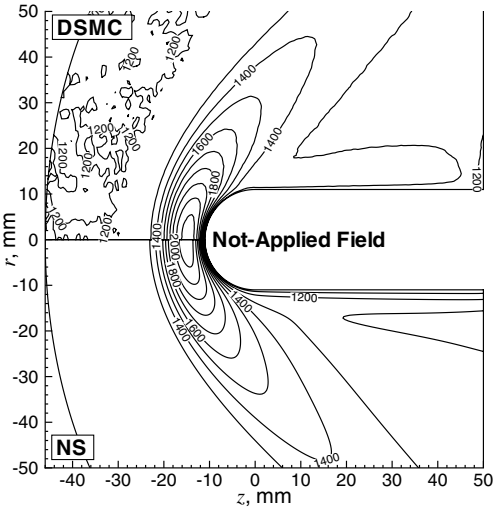

Fig. 5 Temperature contours without B: DSMC (top) and NS computation (bottom); $\Delta T = 100$ K.

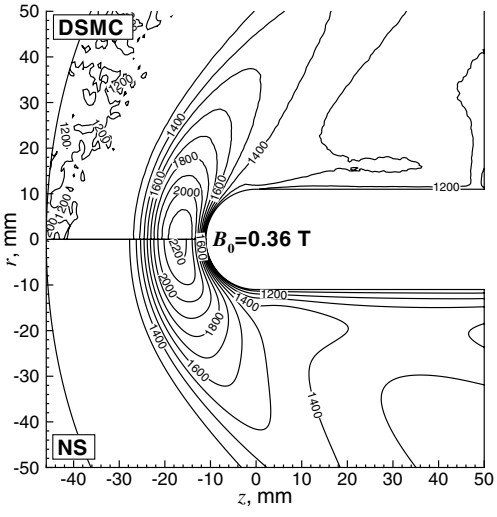

Fig. 6 Temperature contours with $B_0 = 0.36$ T: DSMC (top) and NS computation (bottom); $\Delta T = 100$ K.

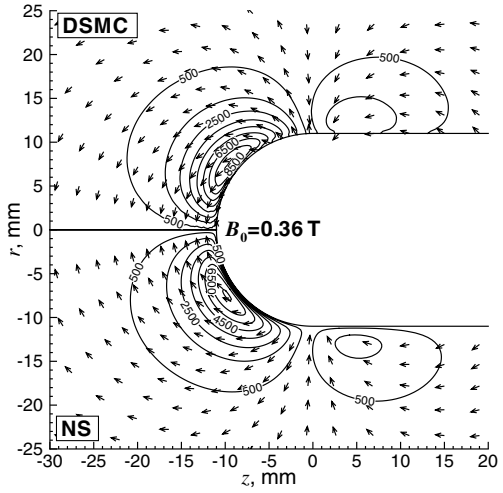

Fig. 7 Lorentz force contours with their directional vectors: DSMC (top) and NS computation (bottom); $\Delta(J \times B) = 1000$ N/m^3.

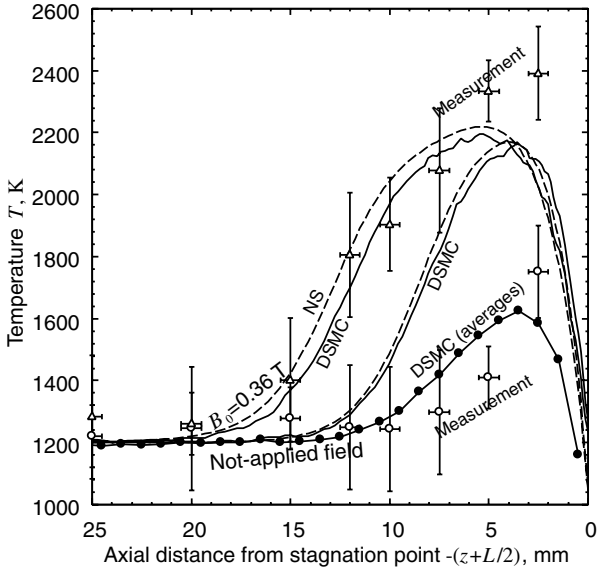

Fig. 8 Comparison of temperature distributions on the axis of symmetry.

be acceptable to reproduce the overall structure of the flow under the present conditions. However, the $\boldsymbol{J} \times \boldsymbol{B}(\propto |\boldsymbol{v}||\boldsymbol{B}^2|)$ term in the DSMC has a slightly larger value near the body surface compared with that in the NS computation, as shown in Fig. 7. This difference also results from the rarefied effect: $|\boldsymbol{v}|$ near the body surface becomes large in the DSMC, because the wall condition is close to that of the slip wall.

In addition, the heat load on the body is estimated by accumulating (time-averaging) the kinetic energy difference of particles at the reflection on the body surface in the DSMC [19] and calculating the heat flux to the body surface in the NS computation. Although the applied field slightly heats up the flow through the Joule heating $\boldsymbol{J} \cdot \boldsymbol{v} \times \boldsymbol{B}$, the increasing shock standoff and the resulting flow diversion from the body reduce the heat flux to the body surface. Net heat load reductions through the applied field are 29.8% in the DSMC and 4.6% in the NS computation. The larger heat load reduction in the DSMC results from a rarefied effect on the cylindrical part: the flow diversion through the applied field reduces the number of particles reflecting on the cylindrical part.

Figure 8 shows the temperature distributions of the DSMC and NS computations on the axis of symmetry and the experimental result [12], which was obtained using the absorption spectroscopy without the Abel inversion. In the case of the applied field, the measured temperature was obtained using a new method [11] that was developed to resolve the distortion of absorption profiles due to the Zeeman effect. Because this method strongly reflects the temperature on the axis of the symmetry, on which the magnetic field is strong [11], both simulated temperatures on the axis of symmetry appear to agree with the measured temperature distribution in the case of the applied field. On the other hand, the measured temperature in the case of the not-applied field cannot be compared directly with the computations, because it would correspond to the average on a laser path. To simulate this averaging effect simply, the computed results are arithmetically averaged from $r = 0$ to L (the approximate plume radius in the experiment) along the laser channel, for which the diameter is 1 mm [11], and the density-weighted temperature T_d

$$T_d = T(n_n/n_{n,0}) \tag{19}$$

is accumulated, because the amount of the laser absorption will be proportional to the population of the lower electronic state of the absorption transition. Herein, $n_{n,0}$ is the neutral argon density on the axis of symmetry. The averaged DSMC temperature is shown in Fig. 8, and it appears to agree with the measured temperature in the case of the not-applied field. Apart from the validity of the averaging effect and the strong temperature reflection of plasma magnetized on the axis of the symmetry in the new measurement method, the standoff distance is irrelevant to these effects, and the computed standoff distances appear to agree with the measurements in both cases of applied and not-applied fields.

B. Drag Exerted on the Body

In this subsection, the simulated drag exerted on the body is compared with the measured drag. In the experiment [13] (using the magnet with $B_0 = 0.4$ T), the total drag D_t was measured using a pendulum apparatus; the drag coefficient C_d increased by 18% through the applied magnetic field. For this study, C_d is defined as

$$C_d = D_t/(q_\infty S) \tag{20}$$

where $q_\infty = m_n n_{n,\infty} v_\infty^2/2$, and $S = \pi(L/2)^2$. Table 2 shows the measured and simulated C_d in the presence and absence of an applied field and their increases through the applied field $\widehat{\Delta C_d}$:

$$\widehat{\Delta C_d} = \frac{C_d(\text{applied field}) - C_d(\text{not-applied field})}{C_d(\text{not-applied field})}, \% \tag{21}$$

The DSMC quantitatively predicts the measured C_d with accuracy of 4% in the case of the not-applied field and qualitatively predicts the measured $\widehat{\Delta C_d}$ with discrepancy overestimated by a factor of 3. On the other hand, the NS computation produces larger C_d than the DSMC in cases of both applied and not-applied fields, but the predicted $\widehat{\Delta C_d}$ is 15% smaller than that of the DSMC.

Table 2 C_d and drag D, mN

Magnetic field	Method	C_d	$\widehat{\Delta C_d}$	D_A	$D_{A,s}$	$D_{A,c}$	ΔD_A	D_L
Not applied	Measurement [13]	2.43 ± 0.06	——	——	——	——	——	——
	DSMC	2.33	——	85.2	52.6	32.6	—	0
	NS	2.71	——	97.1	59.3	37.8	—	0
Applied ($B_0 = 0.4$ T)	Measurement [13]	2.87 ± 0.06	18.1	——	——	——	——	——
	DSMC	3.62	55.4	64.3	41.7	22.6	−20.9	61.1
	NS	3.81	40.5	75.8	48.3	27.5	−21.3	55.7

In fact, D_t is decomposed into the axial component of the aerodynamic drag (i.e., the sum of dynamic pressure and skin friction) and the reaction of the Lorentz force on the magnet to clarify the mechanism of the electromagnetic drag increase.

In the case of the DSMC, the aerodynamic drag D_A is defined as the accumulated (time-averaged) axial momentum difference of particles reflecting on the body surface:

$$D_A = D_{A,s} + D_{A,c} \tag{22}$$

$D_{A,s}$ on the spherical head or $D_{A,c}$ on the cylindrical part are

$$D_{A,s} \text{ or } D_{A,c} = \sum_{n_r} N_w m_n \Delta u_r \Big/ t_e \tag{23}$$

where n_r, t_e, and Δu_r are, respectively, the accumulated number of particles reflecting on the surface during the computation, elapsed time, and the axial velocity difference of a particle through the reflection; DA converges at approximately 20,000 time steps from the initial uniform flow condition.

In the case of the NS computation, using the pressure p and shearing stresses τ_{zz} and τ_{zr} on the body surface, D_A is defined as

$$D_A = -\int_{\text{surface}} p\hat{\boldsymbol{z}} \cdot \mathrm{d}\boldsymbol{S} + \int_{\text{surface}} (\tau_{zz}\hat{\boldsymbol{z}} + \tau_{zr}\hat{\boldsymbol{r}}) \cdot \mathrm{d}\boldsymbol{S} \tag{24}$$

where $\hat{\boldsymbol{r}}$ and $\mathrm{d}\boldsymbol{S}$ are the radial unit vector and the vector area of the body surface. Here, $D_{A,s}$ and $D_{A,c}$ are also calculated separately.

For an applied field, the reaction of the Lorentz force exerted on the magnet is estimated as

$$D_L = -\int_{\text{all cells}} \boldsymbol{J} \times \boldsymbol{B} \mathrm{d}V \tag{25}$$

where $\mathrm{d}V$ is the volume of a cell.

In the simulations, D_t in Eq. (20) was calculated as

$$D_t = D_{A,s} + D_{A,c} + D_L - p_\infty S \tag{26}$$

Table 2 shows each drag component and the variation of D_A (i.e., ΔD_A) through the applied field in the simulations. For no field, $D_{A,c}$ has a value comparable with $D_{A,s}$, because skin friction is predominant in a supersonic rarefied flow [19]. For the applied field, D_A decreases by 21 mN because of the shock layer enlargement, but the generated D_L prominently exceeds its decrease. In the case of the DSMC, D_L therefore occupies approximately 50% of D_t.

Moreover, in contrast to the prediction of the flow structure, the difference between the kinetic and continuum approaches appears in the drag estimation. The NS computation overestimates D_A by 12 mN and underestimates D_L by 5 mN compared with the DSMC, because the velocity slope near the body surface is steep, but its magnitude is small, as a result of the no-slip wall condition. Consequently, the DSMC simulation should be used to estimate drag because of its capability of capturing the rarefied effect near the wall.

C. Possible Causes of the Discrepancy of $\widehat{\Delta C_D}$ Between the Measurement and the DSMC

Despite the correct prediction of C_d (that is, D_A) in the case of the not-applied field, the DSMC fails to predict the measured $\widehat{\Delta C_D}$ quantitatively, which might be the result of ignoring the following effects in computational modeling: 1) the finite radius and nonuniformity of the plume, 2) the rarefied effects originating in charged particles, and 3) the Hall and ion slip effects.

One other possible cause might be the deviation of the actual σ from the value (i.e., 731 S/m) that was estimated using experimentally obtained T_e and α on the central axis on the arcjet plume.

Figure 9 shows variations of D_A, D_L, and $\widehat{\Delta C_d}$ with σ. D_L increases approximately linearly with σ. In contrast, D_A has an opposite tendency, because of the increasing shock layer enlargement. The resulting $\widehat{\Delta C_d}$ increases with σ, because the increase of D_L overwhelms the decrease of D_A. As a result, σ must be reduced to 200 S/m to reproduce the measured $\widehat{\Delta C_d}$.

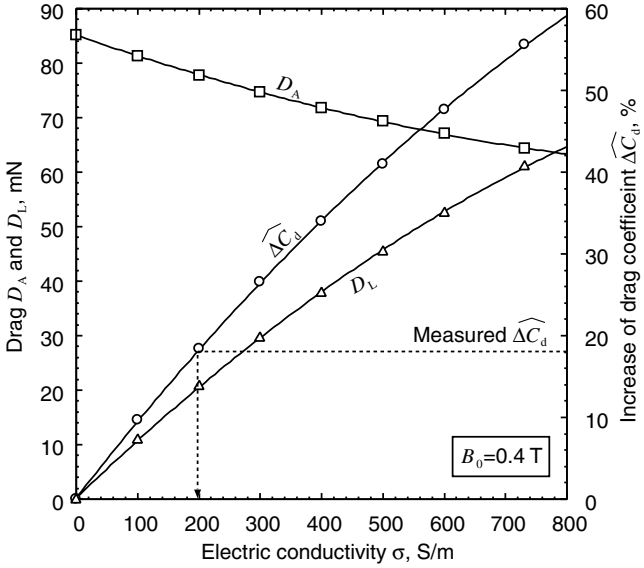

Fig. 9 Variations of D_A, D_L, and $\widehat{\Delta C_d}$ variations with σ: DSMC prediction.

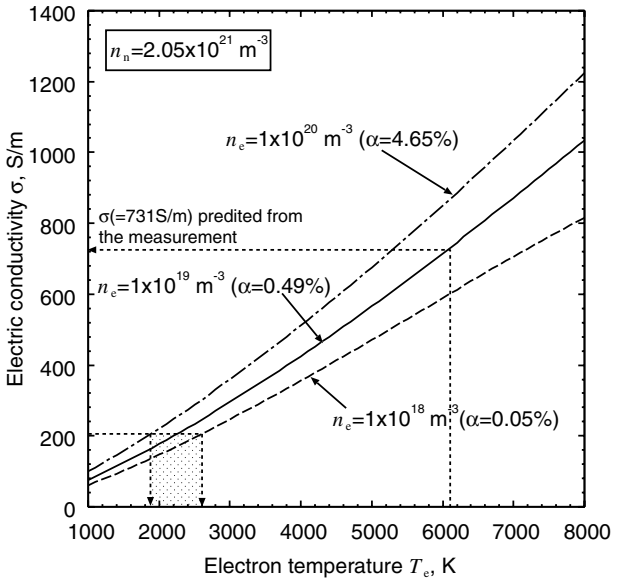

Fig. 10 Electric conductivity σ dependency on T_e and α.

Figure 10 shows the dependence of σ on T_e and n_e. Although σ becomes the reasonable value if T_e is assumed to be about 2000 K, this temperature is too low compared with $T_e = 6100$ K, measured on the central axis of the arcjet plume. Consequently, σ is not the primary cause of the C_d discrepancy. In the experiment, one of the ignored effects (preceding items 1–3) or a multiple effect of them would affect J_θ distribution and the resulting Lorentz force.

V. Conclusions

A weakly ionized rarefied supersonic flow of $K_n = 0.05$ and $M = 1.7$ past a blunt body was simulated using DSMC and NS computation. The electromagnetic effect was investigated by imposing a magnetic field of 0.36–0.4 T around the body. The results computed using respective methods were almost identical in cases in which a field was and was not applied. The continuum approximation is acceptable to reproduce the overall structure of the flow under the present conditions.

Both computations roughly reproduced the measured shock layer enlargement and predicted the resulting reduction of the net heat load on the body.

The DSMC correctly predicted the measured C_d in the case of the not-applied field and qualitatively verified the electromagnetic drag increase measured in the case of the applied field. The electromagnetic effect increases the total drag because the reaction of the generated Lorentz force prominently exceeds the slight decrease of the aerodynamic drag attributable to shock layer enlargement.

Acknowledgments

This research was supported by the Grant-in-Aid for Scientific Research (no. 18206087) and Young Scientists (no. 80435809) from the Japan Society for the Promotion of Science.

References

[1] Kantrowitz, A. R., "A Survey of Physical Phenomena Occurring in Flight at Extreme Speeds," *Proceedings of the Conference on High-Speed Aeronautics*, edited by Ferri, A., Hoff, N. J., and Libby, P. A., Polytechnic Inst. of Brooklyn, Brooklyn, NY, 1955, pp. 335–339.

[2] Resler, E. L., and Sears, W. R., "The Prospects of Magneto-aerodynamics," *Journal of the Aeronautical Sciences*, Vol. 25, No. 4, 1958, pp. 235–245, 258.

[3] Ericson, W. B., and Maciulaitis, A., "Investigation of Magneto-hydrodynamic Flight Control," *Journal of Spacecraft and Rockets*, Vol. 1, No. 3, 1964, pp. 283–289.

[4] Phillips, R. L., "Effect of Magnetic Drag on Re-Entry Body Heating," *American Rocket Society Journal*, Vol. 31, No. 5, 1961, pp. 672–675.

[5] Otsu, H., Matsuda, A., Abe, T., and Konigorski, D., "Feasibility Study on the Flight Demonstration for a Reentry Vehicle with the Magnetic Flow Control System," AIAA Paper 2006-3566, 2006.

[6] Sutton, G. W., and Sherman, A., *Engineering Magnetohydrodynamics*, Dover, New York, 1965.

[7] Ziemer, R. W., and Bush, W. B., "Magnetic Field Effects on Bow Shock Stand-Off Distance," *Physical Review Letters*, Vol. 1, No. 2, 1958, pp. 58–59. doi:10.1103/PhysRevLett.1.58

[8] Ziemer, R. W., "Experimental Investigation in Magneto-Aerodynamics," *American Rocket Society Journal*, Vol. 29, No. 9, 1959, pp. 642–647.

[9] Nowak, R., and Yuen, M. C., "Heat Transfer to a Hemispherical Body in a Supersonic Argon Plasma," *AIAA Journal*, Vol. 11, No. 11, 1973, pp. 1463–1464.

[10] Nowak, R. J., Kranc, S., Porter, R. W., Yuen, M. C., and Cambel, A. B., "Magnetogasdynamic Re-Entry Phenomena," *Journal of Spacecraft and Rockets*, Vol. 4, No. 11, 1967, pp. 1538–1542.

[11] Takizawa, Y., Matsuda, A., Sato, S., Abe, T., and Konigorski, D., "Experimental Investigation of the Electromagnetic Effect on a Shock Layer Around a Blunt Body in a Weakly Ionized Flow," *Physics of Fluids*, Vol. 18, No. 11, 2006, p. 117105. doi:10.1063/1.2375076

[12] Matsuda, A., Wakatsuki, K., Takizawa, Y., Kawamura, M., Otsu, H., Konigorski, D., Sato, S., and Abe, T., "Shock Layer Enhancement by Electro-Magnetic Effect for a Spherically Blunt Body," AIAA Paper 2006-3573, 2006.

[13] Kawamura, M., Matsuda, A., Katsurayama, H., Otsu, H., Konigorski, D., Sato, S., and Abe, T., "Experimental Study on Drag Enhancement in Electrodynamic Heat Shield for a Blunt Body in a Weakly Ionized Plasma Flow," 38th AIAA Plasmadynamics and Lasers Conference, AIAA Paper 2007-3889, 2007.

[14] Poggie, J., and Gaitonde, D. V., "Magnetic Control of Flow past a Blunt Body: Numerical Validation and Exploration," *Physics of Fluids*, Vol. 14, No. 5, 2002, pp. 1720–1731. doi:10.1063/1.1465424

[15] Otsu, H., Abe, T., and Konigorski, D., "Influence of the Hall Effect on the Electrodynamic Heat Shield System for Reentry Vehicles," AIAA Paper 2005-5049, 2005.

[16] Fujino, T., Sugita, H., Mizuno, M., Funaki, I., and Ishikawa, M., "Influences of Electrical Conductivity of Wall on Magnetohydrodynamic Control of Aerodynamic Heating," *Journal of Spacecraft and Rockets*, Vol. 43, No. 1, 2006, pp. 63–70.

[17] Otsu, H., Matsuda, A., Abe, T., and Konigorski, D., "Numerical Validation of the Magnetic Flow Control for Reentry Vehicles," AIAA Paper 2006-3236, 2006.

[18] Hoffert, M. I., and Lien, H., "Quasi-One-Dimensional, Nonequilibrium Gas Dynamics of Partially Ionized Two-Temperature Argon," *Physics of Fluids*, Vol. 10, No. 8, 1967, pp. 1769–1777. doi:10.1063/1.1762356

[19] Bird, G. A., *Molecular Gas Dynamics and the Direct Simulation of Gas Flows*, Oxford Univ. Press, New York, 1994.

[20] Lieberman, M. A., and Lichtenberg, A. J., *Principles of Plasma Discharges and Materials Processing*, 2nd ed., Wiley, New York, 2005.

[21] Gatsonis, N. A., and Yin, X., "Hybrid (Particle-Fluid) Modeling of Pulsed Plasma Thruster Plumes," *Journal of Propulsion and Power*, Vol. 17, No. 5, 2001, pp. 945–958.

[22] Birdsall, C. K., and Langdon, A. B., *Plasma Physics via Computer Simulation*, Inst. of Physics Publishing, Philadelphia, 1991.

[23] Mitchner, M., and Kruger, C. H. Jr., *Partially Ionized Gases*, Wiley, New York, 1973.

[24] Wada, Y., and Liou, M. S., "A Flux Splitting Scheme with High-Resolution and Robustness for Discontinuities," NASA TM 106452, 1994.

[25] Anderson, W. K., Thomas, J. L., and Van Leer, B., "Comparison of Finite Volume Flux Vector Splittings for the Euler Equations," *AIAA Journal*, Vol. 24, No. 9, 1986, pp. 1453–1460.

[26] Van Albada, G. D., Van Leer, B., and Roberts, W. W. Jr., "A Comparative Study of Computational Methods in Cosmic Gas Dynamics," *Astronomy and Astrophysics*, Vol. 108, No. 1, 1982, pp. 76–84.

[27] Jameson, A., and Yoon, S., "Lower-Upper Implicit Schemes with Multiple Grids for the Euler Equations," *AIAA Journal*, Vol. 25, No. 7, 1987, pp. 929–935.

[28] Seldner, D., and Westermann, T., "Algorithms for Interpolation and Localization in Irregular 2D Meshes," *Journal of Computational Physics*, Vol. 79, No. 1, 1988, pp. 1–11. doi:10.1016/0021-9991(88)90001-0

I. Boyd
Associate Editor